In-situ scanning electron microscopy study of fracture events during back-end-of-line microbeam bending tests

K. Vanstreels, I. De Wolf, H. Zahedmanesh, H. Bender, M. Gonzalez, J. Lefebvre, and S. Bhowmick

Citation: Applied Physics Letters **105**, 213102 (2014); doi: 10.1063/1.4902516

View online: http://dx.doi.org/10.1063/1.4902516

View Table of Contents: http://scitation.aip.org/content/aip/journal/apl/105/21?ver=pdfcov

Published by the AIP Publishing

In-situ scanning electron microscopy study of fracture events during back-end-of-line microbeam bending tests

K. Vanstreels,[1,a)] I. De Wolf,[1,2] H. Zahedmanesh,[1] H. Bender,[1] M. Gonzalez,[1] J. Lefebvre,[3] and S. Bhowmick[3]
[1]*Imec, Kapeldreef 75, 3001 Leuven, Belgium*
[2]*Department of Materials Engineering, KU Leuven, 3000 Leuven, Belgium*
[3]*Hysitron, Inc., 9625 West 76th Street, Eden Prairie, Minnesota 55344, USA*

(Received 24 October 2014; accepted 13 November 2014; published online 24 November 2014)

This paper demonstrates the direct observation of crack initiation, crack propagation, and interfacial delamination events during *in-situ* microbeam bending tests of FIB milled BEOL structures. The elastic modulus and the critical force of fracture of the BEOL beam samples were compared for beams of different length and width. © *2014 AIP Publishing LLC*.
[http://dx.doi.org/10.1063/1.4902516]

In order to constantly improve the performance of microelectronic devices and the functionality of advanced integrated circuits, the semiconductor industry is encouraged to introduce alternative materials, processes, chip designs, and packaging strategies into their final products.[1] A good example is the introduction of porous low-*k* dielectrics in the back-end-of-line (BEOL) to reduce the *k*-value needed to prevent leakage between metal interconnections of the circuitry and minimize the time delay. Apart from benefits in lowering the *k*-value, the introduction of porosity inevitably leads to a remarkable degradation of its intrinsic mechanical stability expressed in a decrease of the elastic modulus, interfacial adhesion, and cohesive strength.[2] Besides the need of being compatible with state-of-the-art integration schemes, these materials must also have sufficient mechanical strength to withstand the high shear stresses as well as harsh chemical environments during the chemical mechanical polishing process without cohesive or adhesive failure occurring.[3–5] Moreover, due to the intrinsic tensile stress and increased coefficients of thermal expansion of low-*k* dielectrics compared to SiO_2, thin film cracking and adhesion are serious thermal-mechanical reliability issues for low-*k* dielectric materials.[6,7] Thermo-mechanical deformation of the package during package assembly and subsequent reliability tests can induce large local stresses that can initiate and propagate cohesive and/or adhesive cracks in different BEOL layers.[8] Therefore, a careful characterization of the mechanical stability of potential future low-*k* candidates is required to integrate these materials and Cu interconnects and assures reliability during chip packaging and under field conditions. In the microelectronics industry, the elastic modulus, fracture cohesive strength, and interfacial adhesion of thin continuous films deposited on a silicon substrate are often used to assess the mechanical behavior, fracture behavior, and process compatibility of interlayer dielectric materials. However, these parameters do not sufficiently represent the failure behavior and structure stability of multilevel interconnects, where each material exist as an individual part with different shapes and various cross-section geometries. To gain more insight into root causes of failure processes, the semiconductor industry needs reliable, reproducible testing methods, and strategies to monitor these parameters not only for low-*k* dielectric films but also for complete interconnect stacks. To capture the fracture onset and crack propagation, high-resolution real time techniques are preferred over post mortem observations. Scanning electron microscopy (SEM) is one of the most commonly used techniques for *in-situ* studies, since it yields a high lateral resolution without additional specimen preparation. Three-point microbeam bending is a convenient technique to characterize the elastic response and fracture strength of micro-devices.

In this paper, we demonstrate the direct observation of crack initiation and cohesive and adhesive crack propagation in focused ion-beam (FIB) milled double clamped beam samples of BEOL structures containing seven metal layers using an *in-situ* SEM technique. Figure 1(a) schematically illustrates the FIB milling process of the double clamped BEOL beam samples. First, a clean mill was performed from the cleaved edge, about 5 μm into the silicon substrate, followed by milling a staircase from the other side, leaving somewhat more than the intended beam width (step 1 on Figure 1(a)). Next, the sample was tilted 90° and milled from the cross-section side until the substrate below the BEOL was removed (step 2 on Figure 1(a)). Finally, a clean mill was performed back again to get the target width (step 3 on Figure 1(a)). Figures 1(b)–1(d) show, respectively, a top-down optical image, a cross-sectional optical image, and a SEM image of FIB milled BEOL double clamped beam samples. Four beams with different widths and lengths were fabricated on the same chip at random positions near the cleaved edge (Table I). Due to this, they contained different amounts and orientations of Cu metal lines. A Hysitron PI 85 PicoIndenter equipped with a diamond wedge tip was mounted inside a scanning electron microscope (FEI Versa 3D™) to perform bending tests on the four ion-milled beam samples of BEOL structures. This makes it possible to perform quantitative nano-mechanical testing while simultaneously imaging with the scanning electron microscope. Coupling these two techniques allows to position the probe

[a)]Author to whom correspondence should be addressed. Electronic mail: kris.vanstreels@imec.be

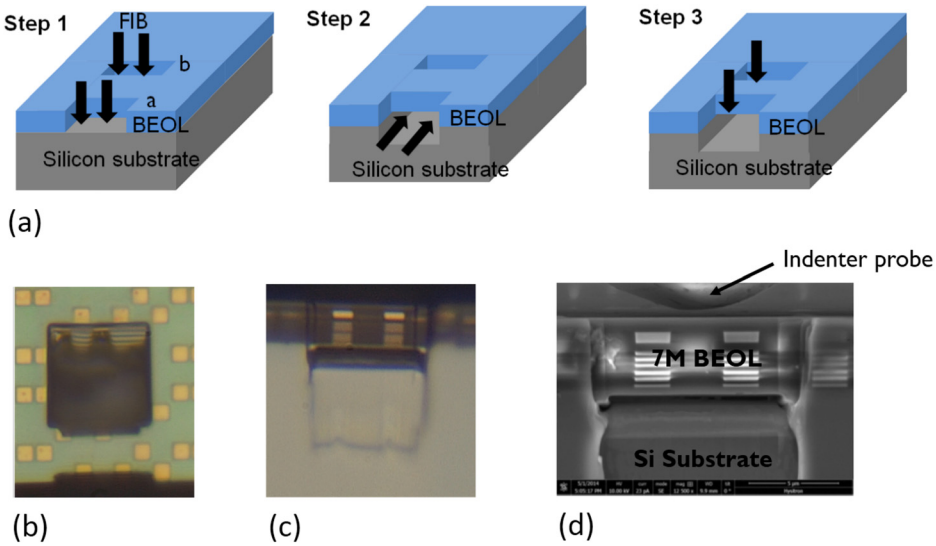

FIG. 1. (a) Schematic overview of the FIB milling process of the double clamped BEOL beam samples; (b) top-down optical image; (c) cross-sectional optical image; and (d) scanning electron microscopy image of FIB-milled beam samples of BEOL structure.

TABLE I. Geometry parameters of the FIB milled beams (length, width, and depth) and the critical load and displacement of fracture.

Beam	Length, L (μm)	Width, b (μm)	Thickness, T (μm)	Loading rate (μN/s)	Critical load (mN)	Critical displacement (nm)
1	9.7	4.4	4.3	750	19.4	513
2	19.1	4.4	4.3	500	9.7	908
3	9.6	2.0	4.1	500	9	534
4	19.1	2.0	4.4	200	4.6	540

with extreme accuracy and image the deformation process throughout the test. All beams were located near a cleaved edge of a silicon chip to allow for imaging of the beam cross-sections while performing the bending tests. The cleaved chip was secured to an instrument-compatible microscopy stub using conductive adhesive, which was then mechanically secured to the stage of the PI 85 for testing. For the bending tests, the wedge was placed in the approximate center of each beam while out of contact and approached until a small force (2 μN) was achieved. The probe was then retracted from the surface to allow for the recovery of any elastic deformation imposed by the small contact force before commencing the loading, which continued until beam failure was achieved. The applied loading rates varied from 200 to 750 μN/s for the various beams. This was done in an attempt to strike a balance between generating failure in a reasonable amount of time, while maintaining the ability to observe the progression of failure in the acquired video. All tests were performed in load-controlled mode. Figure 2 shows a typical force-displacement curve recorded from the *in-situ* beam bending tests and electron micrographs taken at different positions on the force-displacement curve. At a critical force (regions c and d on Figure 2), a crack initiates and further continues to grow in a cohesive and adhesive manner towards the edge of the beam (regions e–g on Figure 2). Figure 3 shows electron micrographs of the various beams acquired before, at critical load, and after the beam bending test. In general, the failure mode for beams 1 and 2 appeared similar as the cracks seem to extend diagonally from the load application site to the underside corners of the beams. Beam 2 also appears to have partial cracking closer to the top side of the beam, as can be seen from the electron micrograph after unloading. The

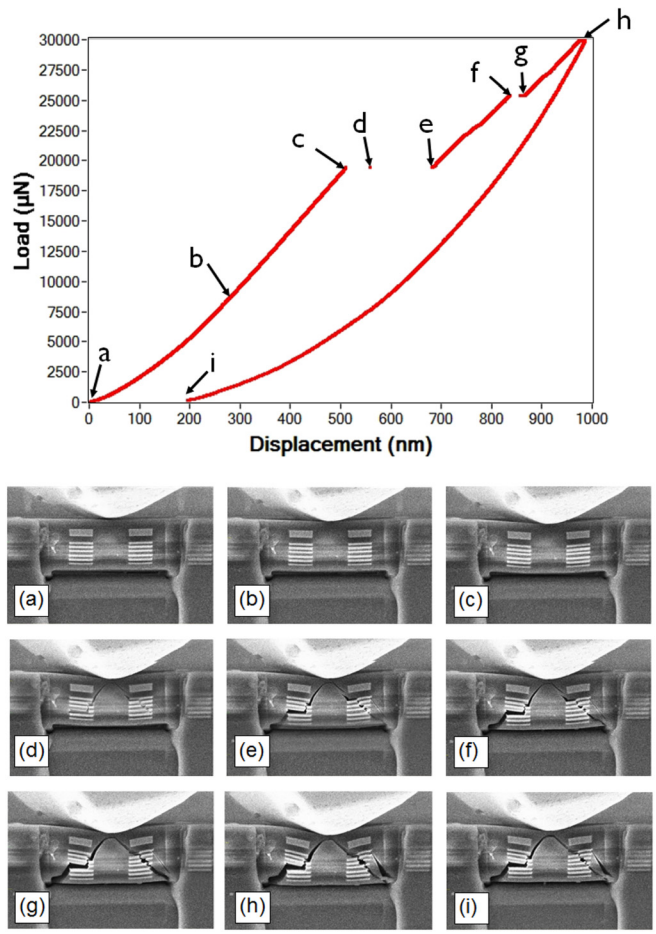

FIG. 2. Typical force-displacement curve recorded from the *in-situ* beam bending tests and corresponding electron micrographs taken at different positions on the force-displacement curve. These micrographs reveal beam bending ((a)–(c)), crack initiation (d), and crack growth ((e)–(h)).

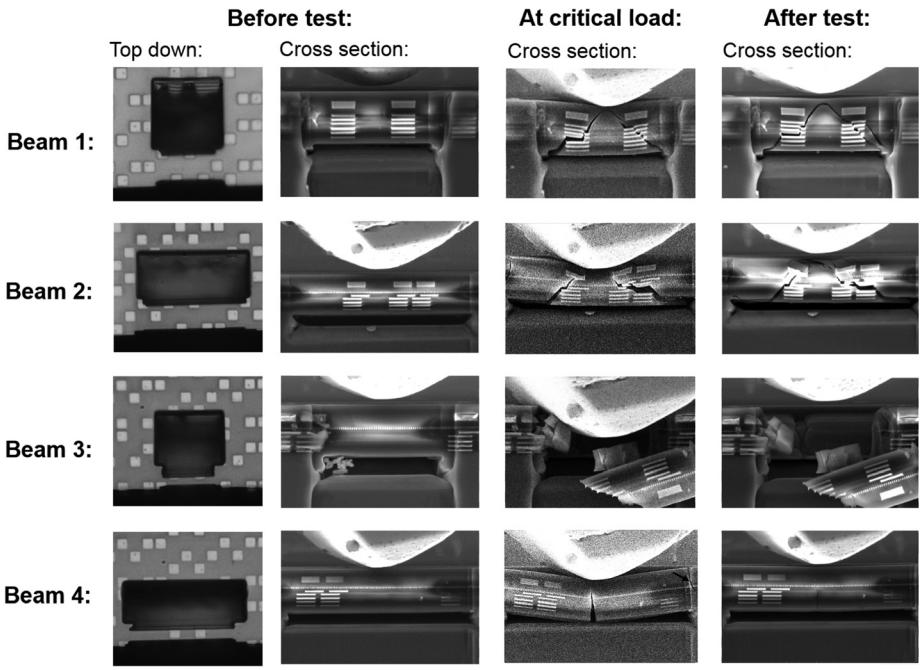

FIG. 3. Electron micrographs of different beams taken before, at critical load, and after the beam bending tests.

failure mode of beam 4 appeared to be different compared to the other tested beams, i.e., a singular crack opening on the bottom side of the beam and progressing towards the point of loading. On this beam there also appeared to be additional cracking to the right side of the image (indicated by an arrow) which is expected to have started at the top of the beam, where the tensile stress is highest. It was difficult to visually inspect the progression of the cracking on beam 3 as it was ejected from its original position upon failure, although the cracks appear to be angular in nature, similar to beam 1. Table I presents the critical force and critical displacement values for each beam. The critical force and displacement values were taken as the force and displacement values just prior to beam fracture, which appears in the force-displacement curves as a discontinuity in displacement with continued loading (regions c–e on Figure 2). It is shown that for beams with a fixed length but different width (beams 1 and 3; beams 2 and 4), a linear dependence of the critical force with the beam width is observed, i.e., the critical load doubles in size when the beam width doubles, as is expected. This is true for both 4.4 μm and 2.0 μm wide beams. Moreover, for beams of similar width, but different length (beams 1 and 2; beams 3 and 4), an inversely dependence of the critical force with the beam length is observed.

To further demonstrate the potential of these experiments, a 2D plane stress finite element (FE) model of beam 4 was developed whereby equivalent Young's modulus and fracture properties of the BEOL were extracted by fitting the parameters of a cohesive zone damage model to recapitulate the force-displacement and crack propagation characteristics observed in the experiments. The extended finite element (XFEM) capability in abaqus FE package (Dassault Systemes, RI) was employed along with a linear cohesive damage model to simulate crack initiation and propagation. Correlating the stress distribution patterns from the FE model to the experiments, for beam 4, clearly supports fracture initiation from locations with highest values of maximum principal stress, as can be seen on Figures 3 and 4.

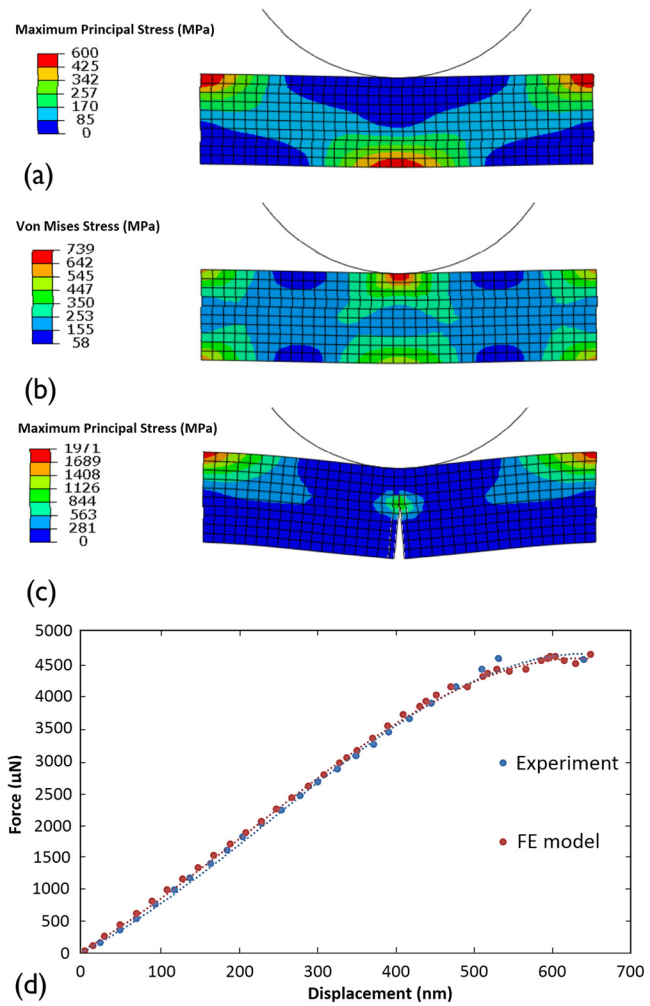

FIG. 4. (a) Maximum principal stress distribution in the microbeam before crack initiation. (b) Distribution of von Mises stress in the microbeam before crack initiation. (c) Maximum principal stress distribution in the microbeam after cessation of the central crack growth. High stress concentration at the top lateral sides of the microbeam is also consistent with the initiation of the secondary crack. (d) Comparison of the experimental and numerical force-displacement response. Force plateau corresponds to the initiation and growth of the central crack.

Therefore, the maximum principal stress based crack initiation criterion was employed in the simulation. Subsequently, the Young's modulus, the value of maximum principal stress for crack initiation and also the fracture energy release rate that resulted in the best agreement between the model and experiments were identified as 39 GPa, 650 MPa, and 1.5 J/m^2, respectively. As shown in Figure 4, a good agreement was obtained between the FE model and the experiments in crack propagation pattern and force-displacement response. Interestingly, in contrast to beam 4, the fracture patterns in beams 1–3 were found to best correlate to von Mises stress distribution (Figures 3 and 4(b)). This point to the existence of two distinct and competing fracture mechanisms, one which is driven only by normal stresses and the other which is driven by shear stress. As to which of the two competing mechanisms prevails is assumed to be dictated by different parameters, including the distribution of copper within the brittle dielectric that renders the beam to follow a brittle or ductile fracture pattern, the loading rate, and the specific beam geometry. However, at this point this is merely a speculation which needs to be further supported by additional experiments.

Even though such analysis based on the structural details of the double clamped BEOL beam samples and the beam bending testing parameters is beyond the scope of this letter, the preliminary results clearly demonstrates the potential of the proposed experiments to mechanistically identify fracture properties and failure mechanisms of BEOL once complemented with simple FE models. Moreover, with further knowledge of the constituents of BEOL and their layout it will be possible to quantitatively identify the weak interfaces and their properties by means of such cross-correlation between fracture patterns in the experiments and models.

In conclusion, this paper demonstrates the direct observation of cohesive and adhesive crack propagation in FIB-milled double clamped beam samples of BEOL structures using an *in-situ* SEM technique. It was found that longer beams result in smaller critical loads, while wider beams result in larger critical loads. Such responses and also the extracted elastic modulus by FEM is assumed to be dictated by the density of copper material that is available in the beams, though remains to be further corroborated upon availability of structural details of the studied BEOL.

[1]K. Maex, M. R. Baklanov, D. Shamiryan, F. Iacopi, S. H. Brongersma, and Z. S. Yanovitskaya, J. Appl. Phys. **93**(11), 8793–8841 (2003).
[2]K. Vanstreels, C. Wu, M. Gonzalez, D. Schneider, D. Gidley, P. Verdonck, and M. R. Baklanov, Langmuir **29**, 12025–12035 (2013).
[3]E. P. Guyer and R. H. Dauskardt, in *IEEE 2003 International Interconnect Technology Conference, Burlingame, CA, USA, 2–4 June 2003* (IEEE, 2003), pp. 89–91.
[4]E. P. Guyer and R. H. Dauskardt, in *IEEE 2004 International Interconnect Technology Conference, Burlingame, CA, USA, 7–9 June 2004* (IEEE, 2004), pp. 236–238.
[5]E. P. Guyer and R. H. Dauskardt, J. Mater. Res. **20**(3), 680–687 (2005).
[6]E. P. Guyer, M. Patz, and R. H. Dauskardt, J. Mater. Res. **21**(4), 882–894 (2006).
[7]T.-S. Kim and R. H. Dauskardt, IEEE Trans. Device Mater. Reliab. **9**(4), 509–515 (2009).
[8]G. Wang, P. S. Ho, and S. Groothuis, Microelectron. Reliab. **45**, 1079–1093 (2005).